X. Spacecraft Control

GUIDANCE AND CONTROL DIVISION

A. The Attitude Control of a Flexible Solar Electric Spacecraft, *E. L. Marsh*

1. Introduction

In keeping with recent advances in solar-electric-powered spacecraft design, a study of the attitude control of such a vehicle during its thrust phase was carried out. The major result of the study was that the influence of large flexible solar arrays was not detrimental to controlling the attitude. It was also determined that "tail-wags-dog" effects on attitude control were minor.

The nonlinear equations of motion for a particular version of a solar-electric-powered spacecraft were detailed in SPS 37-63, Vol. III, pp. 115–122. Figure 1 shows the model for which the equations are valid. B_1 is the rigid spacecraft bus, A is a set of two flexible roll out arrays, and E is the electric engine cluster. The vehicle is designed so that the cluster can translate parallel to either $\mathbf{b}_1$ or $\mathbf{b}_2$, and so that the two outer engines B_3 and B_4 can gimbal about the diagonal along which they lie. Equations of motion for the entire vehicle, the appendage A, the gimballed engines, the translating masses, and the motors that produce gimballing or translating appear in SPS 37-63, Vol. III, pp. 115–122, in Eqs. (2), (5), and (8)–(15). The hybrid coordinates procedure of Likins (Ref. 1) was utilized to account for the dynamics of the flexible solar arrays. A solution of the nonlinear equations of motion is presented in Eq. (16) of SPS 37-63, Vol. III, pp. 115–122.

2. Linear Equations of Motion

The linear variational equations of motion for the system are derived in Ref. 2. For the composite vehicle, the equations are

$$\left.\begin{aligned} I_1\ddot{\theta}_1 + \bar{\kappa}_3 r\ddot{\alpha}_6 - \delta_{51}\ddot{\eta}_5 &= 3\frac{(\mathcal{M}-\bar{m})}{\mathcal{M}} rF\alpha_6 - \frac{3F\Delta_{42}}{\mathcal{M}}\eta_4 \\ I_2\ddot{\theta}_2 - \kappa_3 r\ddot{\alpha}_5 - \delta_{12}\ddot{\eta}_1 &= 3\frac{(\mathcal{M}-m)}{\mathcal{M}} rF\alpha_5 \\ I_3\ddot{\theta}_3 + (\kappa_2 r + I_3^5)\ddot{\alpha}_5 - (\bar{\kappa}_1 r - I_3^6)\ddot{\alpha}_6 - \delta_{23}\ddot{\eta}_2 &= \\ & 2\sqrt{2}p_1^{3*0}F\alpha_3 \end{aligned}\right\} \quad (1)$$

The symbols in these equations are defined in SPS 37-63, Vol. III, or Ref. 2. For the modal coordinates η_i, $i = 1, \cdots, 6$, the following equations are relevant.

$$\left.\begin{aligned} \ddot{\eta}_1 + 2\zeta_1\sigma_1\dot{\eta}_1 + \sigma_1^2\eta_1 &= \delta_{12}\ddot{\theta}_2 \\ \ddot{\eta}_2 + 2\zeta_2\sigma_2\dot{\eta}_2 + \sigma_2^2\eta_2 &= \delta_{23}\ddot{\theta}_3 \\ \ddot{\eta}_3 + 2\zeta_3\sigma_3\dot{\eta}_3 + \sigma_3^2\eta_3 &= 0 \\ \ddot{\eta}_4 + 2\zeta_4\sigma_4\dot{\eta}_4 + \sigma_4^2\eta_4 &= -\Delta_{42}r\ddot{\alpha}_6 \\ \ddot{\eta}_5 + 2\zeta_5\sigma_5\dot{\eta}_5 + \sigma_5^2\eta_5 &= \delta_{51}\ddot{\theta}_1 \\ \ddot{\eta}_6 + 2\zeta_6\sigma_6\dot{\eta}_6 + \sigma_6^2\eta_6 &= 0 \end{aligned}\right\} \quad (2)$$

Either of the gimballing engine's equations has the form

$$I_1^3\left[\ddot{\alpha}_3+\frac{1}{\sqrt{2}}(\ddot{\theta}_1+\ddot{\theta}_2)\right]+d_3\ddot{\alpha}_3-k_3(\alpha_{G1}-\alpha_3)=0 \tag{3}$$

While for the translator,

$$\left.\begin{aligned}
&\left(I_3^5+mr^2+\frac{m^3r^2}{\mathcal{M}^2}-2\frac{m^2r^2}{\mathcal{M}}\right)\ddot{\alpha}_5+r^2d_1\dot{\alpha}_5+k_2\alpha_5+\frac{m^2\bar{m}}{\mathcal{M}^2}r^2\ddot{\alpha}_6-k_2\alpha_{T2}+\left(\frac{mr\mu}{\mathcal{M}}-\mu r\right)\ddot{\theta}_2+I_3^5\ddot{\theta}_3=0\\
&\left(I_3^6+\bar{m}r^2+\frac{m\bar{m}^2}{\mathcal{M}^2}r^2-2\frac{\bar{m}^2}{\mathcal{M}}r^2\right)\ddot{\alpha}_6+r^2d_1\dot{\alpha}_6+k_1\alpha_6+\frac{m^2\bar{m}}{\mathcal{M}^2}r^2\ddot{\alpha}_5-\frac{1}{\mathcal{M}}\left(\frac{m\bar{m}}{\mathcal{M}}r-\bar{m}r\right)\Delta_{42}\ddot{\eta}_4-k_1\alpha_{T1}\\
&\qquad-\left(\frac{\bar{m}r\mu}{\mathcal{M}}-\bar{\mu}r\right)\ddot{\theta}_1+I_3^6\ddot{\theta}_3=0
\end{aligned}\right\} \tag{4}$$

3. Control

Differential equations associated with the control system are

$$\tau_{Si}\dot{V}_{Si}+V_{Si}=K_{Si}\theta_i,\qquad i=1,2,3 \tag{5}$$

$$\left.\begin{aligned}
r\dot{\alpha}_{T1}&=K_{M1}K_{V1}(V_{S1}-V_{F1})\\
r\dot{\alpha}_{T2}&=K_{M2}K_{V2}(-V_{S2}-V_{F2})\\
\dot{\alpha}_G&=K_{M3}K_{V3}(V_{S3}-V_{F3})
\end{aligned}\right\} \tag{6}$$

$$\left.\begin{aligned}
\ddot{V}_{F1}&=\frac{K_{F1}K_{11}K_{M1}K_{V1}}{\tau_{11}\tau_{21}}\left[\frac{\tau_{21}}{\tau_{S1}}K_{S1}\theta_1+\left(1+K_{21}-\frac{\tau_{21}}{\tau_{S1}}\right)V_{S1}-\left(\tau_{21}+\frac{\tau_{11}+\tau_{21}}{K_{F1}K_{11}K_{M1}K_{V1}}\right)\dot{V}_{F1}\right.\\
&\qquad\left.-\left(1+K_{21}+\frac{1}{K_{F1}K_{11}K_{M1}K_{V1}}\right)V_{F1}\right]\\
\ddot{V}_{F2}&=-\frac{K_{F2}K_{12}K_{M2}K_{V2}}{\tau_{12}\tau_{22}}\left[\frac{\tau_{22}}{\tau_{S2}}K_{S2}\theta_2+\left(1+K_{22}-\frac{\tau_{22}}{\tau_{S2}}\right)V_{S2}+\left(\tau_{22}+\frac{\tau_{12}+\tau_{22}}{K_{F2}K_{12}K_{M2}K_{V2}}\right)\dot{V}_{F2}\right.\\
&\qquad\left.+\left(1+K_{22}+\frac{1}{K_{F2}K_{12}K_{M2}K_{V2}}\right)V_{F2}\right]\\
\ddot{V}_{F3}&=\frac{K_{F3}K_{13}K_{M3}K_{V3}}{\tau_{13}\tau_{23}}\left[\frac{\tau_{13}}{\tau_{S3}}K_{S3}\theta_3+\left(1+K_{23}-\frac{\tau_{23}}{\tau_{S3}}\right)V_{S3}-\left(\tau_{23}+\frac{\tau_{13}+\tau_{23}}{K_{F3}K_{13}K_{M3}K_{V3}}\right)\dot{V}_{F3}\right.\\
&\qquad\left.-\left(1+K_{23}+\frac{1}{K_{F3}K_{13}K_{M3}K_{V3}}\right)V_{F3}\right]
\end{aligned}\right\} \tag{7}$$

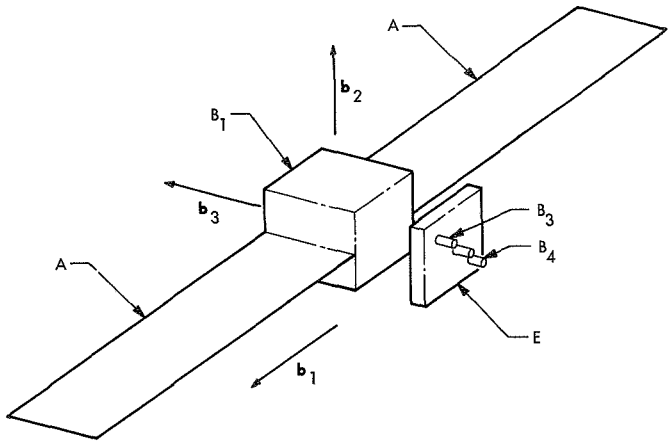

Fig. 1. Solar-electric-powered spacecraft

New symbols introduced here are defined in Ref. 2. In the parametric stability analysis which follows, K_{Si}, $i = 1, 2, 3$, was the only parameter varied. Figure 2 is the block diagram representation of Expressions (1)–(7).

The dashed lines indicate coupling terms. Solid lines are associated with the uncoupled equations. The mode shapes corresponding to the modes excited by rotation about each axis are drawn at the right of the block diagram. The third and sixth modes are absent. This is predictable from Expression (2), which indicates that the third and sixth modes of structural vibration decouple from the remaining equations and have no effect on the attitude motion.

4. Stability Analysis

Only the uncoupled equations were considered in the first part of the stability analysis. This uncoupling transforms the attitude control problem into one that is amenable to root locus analysis. In addition to uncoupling, the high-frequency translator and gimballing dynamics were omitted from the initial stability analysis. This system where coupling and translator and gimballing dynamics are omitted will be referred to as the modified system.

The open loop transfer functions for the three axes are

$$G_1H_1 = -\bar{\kappa}_3K_{S1}K_{M1}K_{V1}\,(s^6 + N_5s^5 + N_4s^4 + N_3s^3 + N_2s^2 + N_1s + N_0)\left(s + \frac{1}{\tau_{21}}\right)\left(s + \frac{1}{\tau_{11}}\right)\Big/(I_1 - \delta_{51}^2)$$
$$\times\,\tau_{S1}s^3\,(s^4 + D_3s^3 + D_2s^2 + D_1s + D_0)\left(s + \frac{1}{\tau_{S1}}\right)\left\{s^2 + \frac{1}{\tau_{21}\tau_{11}}\left[\tau_{11} + (1 + K_{11}K_{M1}K_{V1}K_{F1})\,\tau_{21}\right]\right.$$
$$\left.\times\,s + \frac{1}{\tau_{21}\tau_{11}} + \frac{K_{11}K_{M1}K_{V1}K_{F1}}{\tau_{21}\tau_{11}}(1 + K_{21})\right\} \qquad (8)$$

$$G_2H_2 = -\frac{\kappa_3K_{S2}K_{M2}K_{V2}}{(I_2 - \delta_{12}^2)}\left[s^2 + 3\frac{(\mathcal{M} - m)}{\kappa_3\mathcal{M}}F\right](s^2 + 2s\zeta_1\sigma_1 + \sigma_1^2)\left(s + \frac{1}{\tau_{22}}\right)\left(s + \frac{1}{\tau_{12}}\right)\Big/s^3\left(s^2 + \frac{2I_2}{I_2 - \delta_{12}^2}\right.$$
$$\left.\times\,\zeta_1\sigma_1s + \frac{I_2\sigma_1^2}{I_2 - \delta_{12}^2}\right)\left(s + \frac{1}{\tau_{S2}}\right)\left\{s^2 + \frac{1}{\tau_{22}\tau_{12}}\left[\tau_{12} + (1 + K_{21}K_{M2}K_{V2}K_{F2})\,\tau_{22}\right]\right.$$
$$\left.\times\,s + \frac{1}{\tau_{22}\tau_{12}} + \frac{K_{12}K_{M2}K_{V2}K_{F2}}{\tau_{22}\tau_{12}}(1 + K_{22})\right\} \qquad (9)$$

$$G_3H_3 = -\frac{\sqrt{8}\,p_1^{3*0}FK_{S3}K_{M3}K_{V3}}{(I_3 - \delta_{23}^2)\,\tau_{S3}}(s^2 + 2\zeta_2\sigma_2s + \sigma_2^2)\left(s + \frac{1}{\tau_{23}}\right)\left(s + \frac{1}{\tau_{13}}\right)\Big/s^3\left(s^2 + \frac{2I_3\zeta_2\sigma_2}{I_3 - \delta_{23}^2} + \frac{I_3\sigma_2^2}{I_3 - \delta_{23}^2}\right)$$
$$\times\left(s + \frac{1}{\tau_{S3}}\right)\left\{s^2 + \frac{1}{\tau_{23}\tau_{13}}\left[\tau_{13} + (K_{M3}K_{F3}K_{13}K_{V3} + 1)\,\tau_{23}\right]s + \frac{1}{\tau_{23}\tau_{13}} + \frac{K_{F3}K_{M3}K_{13}K_{V3}}{\tau_{23}\tau_{13}}(1 + K_{23})\right\} \qquad (10)$$

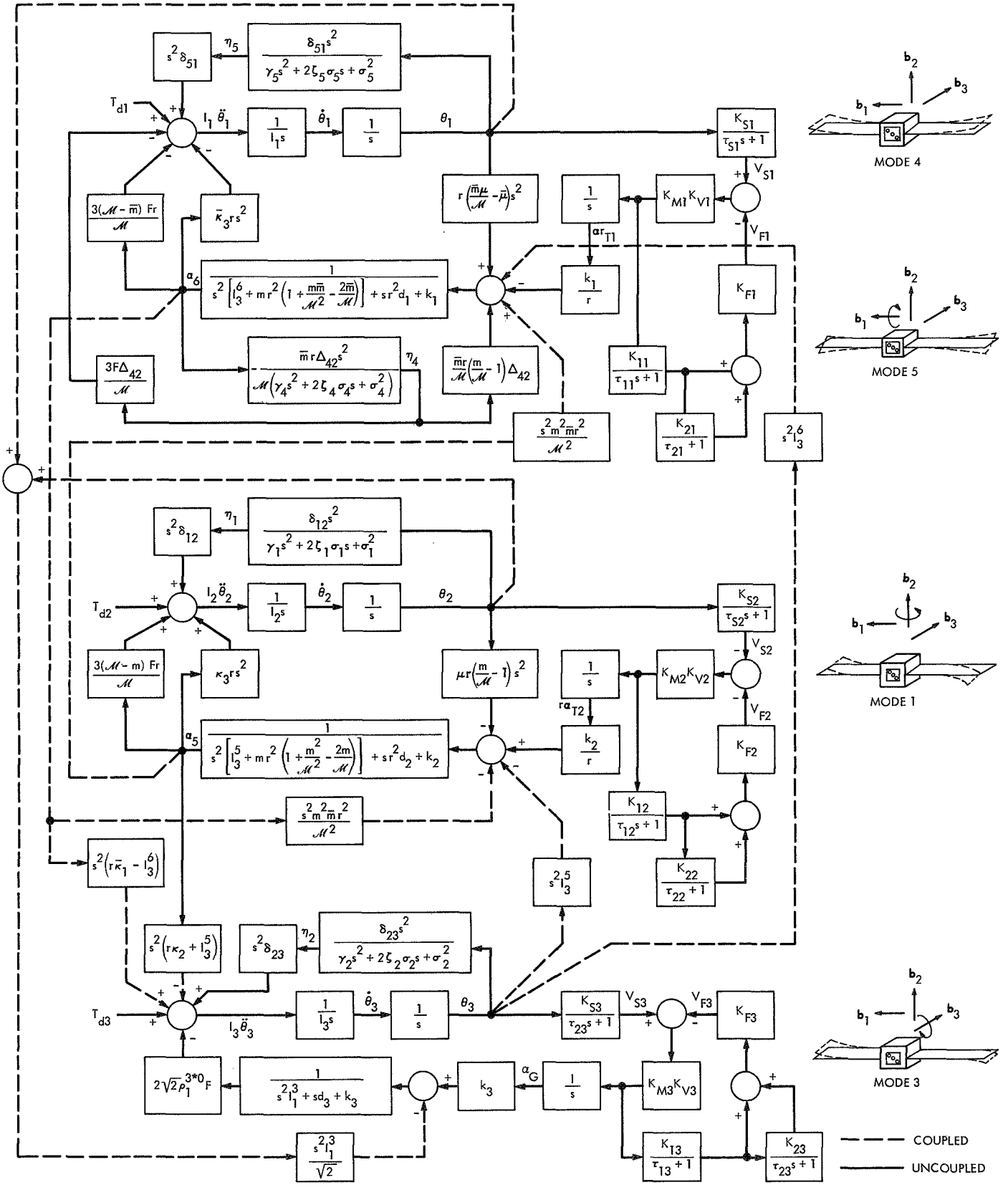

Fig. 2. Block diagram for coupled and uncoupled equations, including mode shapes

where G_i is the forward loop transfer function and H_i is the feedback loop transfer function for the axis parallel to $\mathbf{b}_i$. Expressions for N_i, $i = 0, \cdots, 5$, and for D_j, $j = 0, \cdots, 3$, are

$$
\left.
\begin{aligned}
N_5 &= 2(\zeta_4\sigma_4 + \zeta_5\sigma_5) \\
N_4 &= \sigma_4^2 + \sigma_5^2 + 4\zeta_4\zeta_5\sigma_4\sigma_5 + \frac{3(\mathcal{M} - \bar{m})F}{\bar{\kappa}_3\mathcal{M}} - \frac{3F\bar{m}\Delta_{42}^3}{\bar{\kappa}_3\mathcal{M}^2} \\
N_3 &= 2\sigma_4\sigma_5(\zeta_4\sigma_5 + \zeta_5\sigma_4) + \frac{6(\mathcal{M} - \bar{m})}{\bar{\kappa}_3\mathcal{M}}(\zeta_4\sigma_4 + \zeta_5\sigma_5) \\
&\quad - \frac{6F\bar{m}\Delta_{42}^2\zeta_5\sigma_5}{\bar{\kappa}_3\mathcal{M}^2} \\
N_2 &= \sigma_4^2\sigma_5^2 + \frac{3(\mathcal{M} - \bar{m})}{\bar{\kappa}_3\mathcal{M}}(\sigma_4^2 + \sigma_5^2 + 4\zeta_4\zeta_5\sigma_4\sigma_5) \\
&\quad - \frac{3F\bar{m}\Delta_{42}^2\sigma_5^2}{\bar{\kappa}_3\mathcal{M}^2} \\
N_1 &= \frac{6(\mathcal{M} - \bar{m})F\sigma_4\sigma_5}{\bar{\kappa}_3\mathcal{M}}(\zeta_4\sigma_5 + \zeta_5\sigma_4) \\
N_0 &= \frac{3(\mathcal{M} - \bar{m})F\sigma_4^2\sigma_5^2}{\bar{\kappa}_3\mathcal{M}}
\end{aligned}
\right\} \quad (11)
$$

and

$$
\left.
\begin{aligned}
D_3 &= \frac{I_1}{I_1 - \delta_{51}^2}\left[2(\zeta_4\sigma_4 + \zeta_5\sigma_5) - \frac{2\delta_{51}^2\zeta_4\sigma_4}{I_1}\right] \\
D_2 &= \frac{I_1}{I_1 - \delta_{51}^2}\left(\sigma_4^2 + \sigma_5^2 + 4\zeta_4\zeta_5\sigma_4\sigma_5 - \frac{\delta_{51}^2\sigma_4^2}{I_1}\right) \\
D_1 &= \frac{2I_1\sigma_4\sigma_5}{I_1 - \delta_{51}^2}(\zeta_4\sigma_5 + \zeta_5\sigma_4) \\
D_0 &= \frac{I_1\sigma_4^2\sigma_5^2}{I_1 - \delta_{51}^2}
\end{aligned}
\right\} \quad (12)
$$

Values selected for the parameters in these expressions, as well as for the parameters in Expressions (1)–(10), are

$$
\begin{aligned}
K_{1i} &= 100 \text{ V-s/ft}, \qquad i = 1, 2, 3 \\
K_{2i} &= 4.5 \qquad i = 1, 2, 3 \\
K_{Fi} &= 80 \qquad i = 1, 2, 3 \\
K_{M1} &= K_{M2} = 2.2 \times 10^{-4} \text{ ft/pulse} \\
K_{M3} &= 10^{-4} \text{ rad/pulse} \\
K_{Vi} &= 40 \text{ pulses/V-s}, \qquad i = 1, 2, 3
\end{aligned}
$$

$$
\begin{aligned}
\delta_{23} &= 94.51 \text{ slug-ft}^2 \\
\delta_{12} &= 94.60 \text{ slug-ft}^2 \\
\delta_{51} &= 7.084 \text{ slug-ft}^2 \\
\Delta_{42} &= 3.077 \text{ slug-ft} \\
\zeta_i &= 0.005 \text{ slug}^{1/2}\text{-ft}, \qquad i = 1, 2, 3, 4, 5 \\
\sigma_1 &= 0.02129 \text{ slug}^{1/2}\text{-ft/s} \\
\sigma_2 &= 0.02141 \text{ slug}^{1/2}\text{-ft/s} \\
\sigma_4 &= 0.02376 \text{ slug}^{1/2}\text{-ft/s} \\
\sigma_5 &= 0.02838 \text{ slug}^{1/2}\text{-ft/s} \\
\tau_{1i} &= 10^3 \text{ s}, \qquad i = 1, 2, 3 \\
\tau_{2i} &= 5 \times 10^2 \text{ s}, \qquad i = 1, 2, 3 \\
\tau_{Si} &= 1 \text{ s}, \qquad i = 1, 2, 3 \\
F &= 0.02 \text{ lb} \\
I_1 &= 326.4 \text{ slug-ft}^2 \\
I_2 &= 9420.0 \text{ slug-ft}^2 \\
I_3 &= 9148.0 \text{ slug-ft}^2 \\
M &= 41.09 \text{ slug} \\
m &= 3.727 \text{ slug} \\
\bar{m} &= 3.106 \text{ slug} \\
\bar{\kappa}_3 &= -9.318 \text{ slug-ft} \\
\kappa_3 &= -7.765 \text{ slug-ft}
\end{aligned}
$$

The sensor gains K_{Si} have not been specified and will serve as variable parameters upon which the attitude stability depends.

A root locus diagram for the $\mathbf{b}_1$ axis appears in Fig. 3. Values for the open loop poles and zeros are given. Poles and zeros having non-zero imaginary parts are associated with the fourth and fifth modes. A real zero at 0.084324 is due to the so-called "tail wags dog" effect, or the term $\bar{\kappa}_3 r\ddot{\alpha}_6$ in the first of Expression (1). This is an inertia torque exerted on the vehicle when the engine cluster unit translates parallel to the $\mathbf{b}_2$ vector. Such motion excites fourth-mode oscillations. Figure 4 is an enlarged version of the $\mathbf{b}_1$ axis root locus and shows detail near the origin. For very small gain, i.e., very small K_{S1}, the locus emanating from the multiple pole at zero initially passes into the right half plane. Thus, instability is implied. As K_{S1} is increased, the locus crosses back into the left half plane and finally returns to the right half plane for sufficiently large K_{S1}. The range of K_{S1} for which all parts of the locus lie in the left half plane, i.e., for which stability is guaranteed for the $\mathbf{b}_1$ axis, is $0.5 < K_{S1} < 23$.

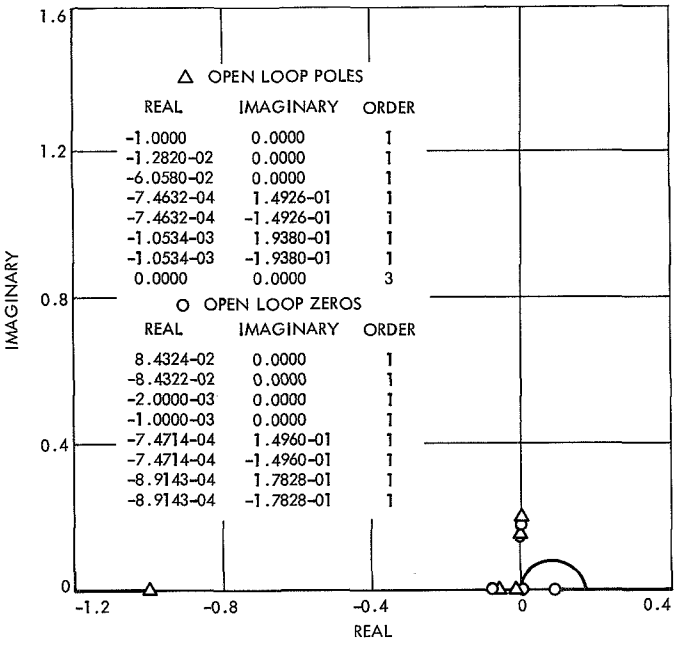

Fig. 3. b_1-axis root locus

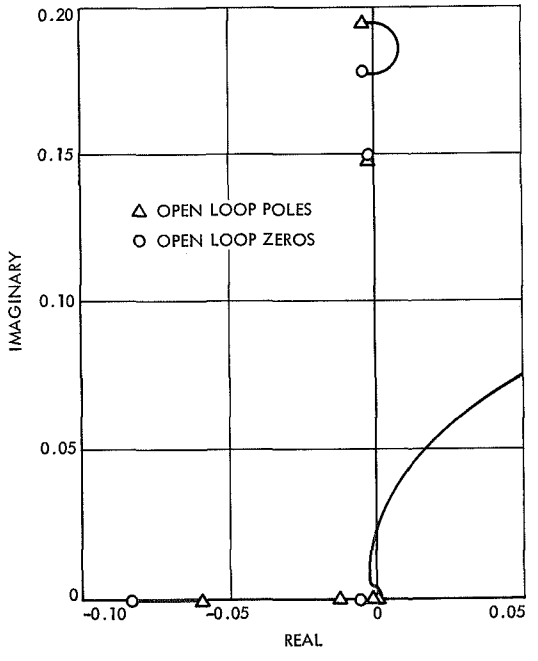

Fig. 4. Enlarged b_1-axis root locus

Similar analyses were conducted for the b_2 and b_3 axes. The stable ranges for K_{S2} and K_{S3} are

$$15 < K_{S2} < 201$$

$$11 < K_{S3} < 221$$

The effect of the flexible solar arrays was assessed by performing root locus analyses for the rigid spacecraft models. The resulting stable K_{Si}, $i = 1, 2, 3$, ranges were

$$0.52 < K_{S1} < 23.52$$

$$16 < K_{S2} < 276$$

$$11 < K_{S3} < 221$$

Comparison with the values for the non-rigid case shows that only the b_2 axis results are appreciably modified when flexibility is taken into account.

Time histories of the attitude angles θ_1, θ_2, and θ_3 appear in Figs. 5 and 6. The continuous system simulation language (CSSL), developed through support of the Guidance and Control Branch of the Office of Advanced Research and Technology, was used in programming the linear equations for the Univac 1108 digital computer. For the axis parallel to b_i, the initial attitude angle rate $\dot{\theta}_i$ is 10^{-4} rad/s. This rate is considerably larger than those expected to be encountered from disturbance torques for a deep space mission. All other variables, i.e., θ_i, V_{Si}, etc., have an initial value of zero.

Figure 5 shows the attitude behavior for cases when K_i, $i = 1, 2, 3$, is in the stable range stated earlier, in particular, $K_{S1} = 20$, $K_{S2} = 100$, $K_{S3} = 100$. At approximately 100 s, θ_1 reaches its maximum amplitude of 6.4×10^{-3} rad. For a time of 2800 s, the amplitude has diminished to nearly 7×10^{-4} rad or one-tenth the maximum amplitude. For θ_2 and θ_3, the response curves are of a lower frequency than for θ_1.

Values for K_{S1}, K_{S2}, and K_{S3} in Fig. 6 are 50, 350, and 350, respectively. These fall outside of the stable range. The θ_i responses are then expected to be unstable. This is seen to be the case. However, the curves are not reliable as true indicators of the behavior of θ_i since the linear equations are not really valid for large θ_i. θ_i is indeed unstable, but its time history probably departs markedly from the curves of Fig. 6.

Following the root locus analysis, a stability analysis for the coupled system of equations (including the translator and gimballing dynamics) was undertaken. For linear systems, stability is guaranteed whenever the eigenvalues are distinct and have negative real parts. For the case at hand, the system of first- and second-order linear differential equations was converted to a system of first-order differential equations of the form

$$\dot{X} = AX \tag{13}$$

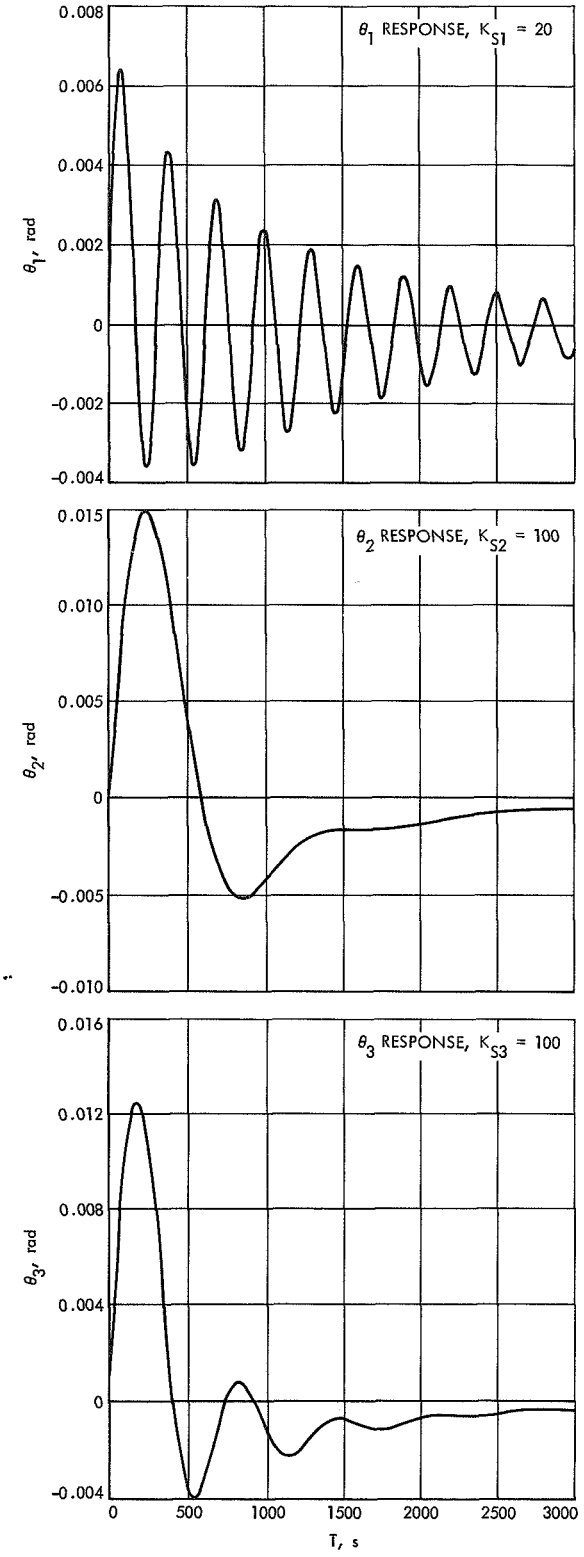

Fig. 5. Response curves in stable range

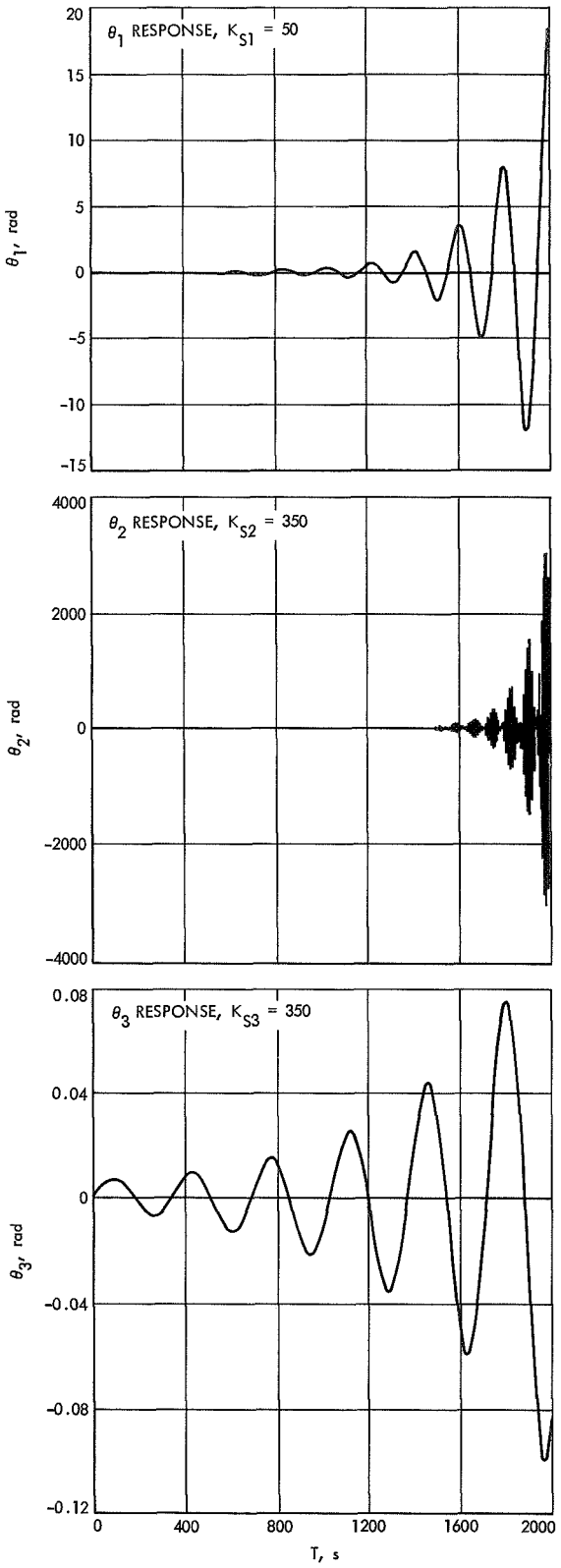

Fig. 6. Response curves outside stable range

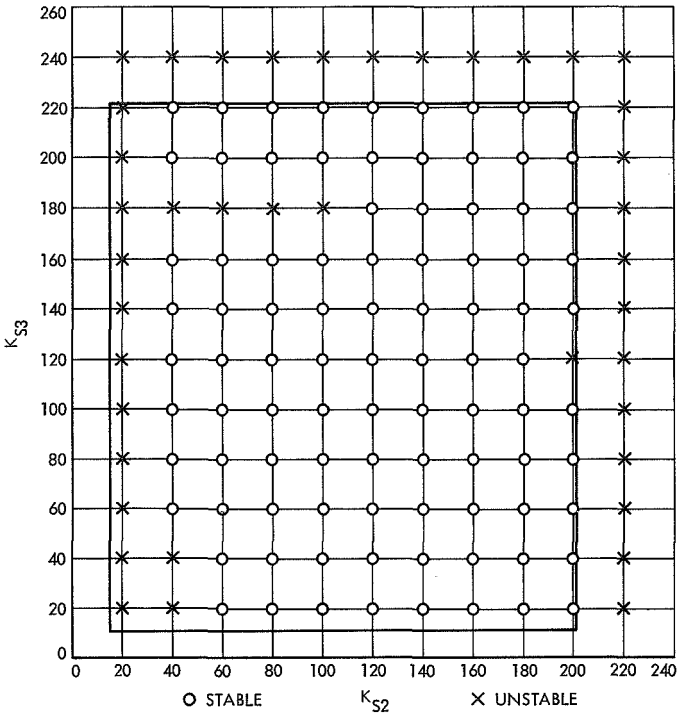

Fig. 7. Stability chart for modified and unmodified systems ($K_{S1} = 10$)

where X is a 32×1 vector and A is a 32×32 matrix. Determination of the eigenvalues for the system is equivalent to determining the eigenvalues for A. Figure 7 shows the results of the eigenvalue analysis. The value for K_{S1} was fixed at 10. Figure 7 presents stability information for both the modified and the unmodified systems. The region enclosed by the rectangle, i.e., $15 < K_{S2} < 201$ and $11 < K_{S3} < 221$, is, for $K_{S1} = 10$, the stability zone for the modified system. Any K_{S2} or K_{S3} value falling in that zone is such that stability for the modified system is guaranteed. The eigenvalue analysis determined that some minor alteration of the boundaries is required when coupling and translator and gimballing dynamics are accounted for. Each grid intersection point in Fig. 7 was investigated for stability for the unmodified system. For small values of K_{S2}, it was found that configurations which were formerly stable for the modified system are unstable. Instabilities in the vicinity of $K_{S3} = 180$ also appear. A more detailed analysis of this region showed that instabilities were not restricted to $K_{S3} = 180$.

5. Conclusions

The work presented here has demonstrated the feasibility of using electric propulsion engines for attitude control as well as for propulsion during the low-thrust cruise phase of a deep space mission. In addition, it has been shown that flexibility associated with large roll-out solar arrays poses no great threat to the success of such missions. Furthermore, the detrimental effects from torques due to "tail-wags-dog" terms can be offset.

References

1. Likins, P. W., *Dynamics and Control of Flexible Space Vehicles,* Technical Report 32-1329 (Revision 1). Jet Propulsion Laboratory, Pasadena, Calif., Jan. 15, 1970.

2. Marsh, E. L., *The Attitude Control of a Flexible Solar Electric Spacecraft,* paper presented at the AIAA 8th Electric Propulsion Conference, Stanford, Calif., Aug. 31–Sept. 2, 1970.

B. Finite Element Modeling for Appendage Interaction With Spacecraft Control, P. W. Likins[1] and E. L. Marsh

1. Introduction

Useful analyses of the spacecraft attitude control/structural dynamics interaction problem can be carried out when accurate models of the attitude control system and the spacecraft dynamics are available. For the spacecraft dynamics, a hybrid coordinates model, utilizing discrete coordinates for rigid body kinematics and modal coordinates related to the elastic structure's deformation coordinates, has been suggested by Likins.

The basic hybrid coordinates philosophy is adhered to in this article. However, a detailed description of an improved model[2] for the flexible components is discussed. For the model currently in use at JPL (Ref. 1), flexible appendages are approximated by an array of rigid finite bodies connected by massless elastic beams. The improved model consists of a collection of finite elastic elements possessing mass and interconnected at points where finite rigid masses may be located. The points of connection and the masses at these points are referred to as nodes and nodal bodies respectively. In the following discussion, equations of motion for the finite elements, the rigid bodies, and the composite appendage will be stated. These must be used in conjunction with the vehicle equations and the control system equations in order to properly analyze the spacecraft dynamics and control interaction problem.

2. Appendage Idealization

Figure 1 shows the two basic types of units considered in the analysis. Body b is a rigid body and a is a flexible appendage. For a real vehicle, these may represent the spacecraft bus and a solar panel, respectively. The tetrahedral object having dotted lines for boundaries and with parallelepipeds at its vertices represents the typical finite element s and nodal bodies as described above. Shapes other than tetrahedrons and parallelepipeds may be assumed for the finite elements and nodal bodies. The deformed tetrahedron having dashed line boundaries indicates the steady-state deformation which may be imposed by a constant rotation of a in inertial space. Finally, the deformed version of the finite element having solid line boundaries represents the configuration for an excited state where both steady-state and oscillatory deformations occur.

Unit vectors fixed in b are $\mathbf{b}_i$, $i = 1, 2, 3$. Unit vectors fixed in the undeformed appendage are $\mathbf{a}_i$. Q is a point on the a–b interface. O and O' locate the vehicle mass center in the steady state and undeformed state, respectively. The mass center for a general oscillatory state is CM. The meanings of other symbols in Fig. 1 are either self evident or are described in *Section D*, Ref. 1, or will be described in the sequel.

3. Finite Element Equation of Motion

This equation is established by equating the work W^* done by external forces in the course of a virtual displacement of the nodes to the strain energy U^* stored in the deforming element. The nodal displacement vector $\bar{y}$ for the element in consideration is defined by

$$\bar{y} = \begin{bmatrix} \bar{u}^k \\ \bar{\beta}^k \\ \bar{u}^i \\ \bar{\beta}^i \\ \cdot \\ \cdot \\ \cdot \\ \bar{u}^j \\ \bar{\beta}^j \end{bmatrix} \tag{1}$$

where $\bar{u}^k$ and $\bar{\beta}^k$ are the 3×1 translational and rotational deformation vectors, respectively, for the kth node of element s and expressed in terms of local coordinates ξ, η, ζ parallel to $\mathbf{e}_1$, $\mathbf{e}_2$, $\mathbf{e}_3$, which are unit vectors fixed in the steady-state configuration for the element. Whenever a vector is expressed in terms of local coordinates, it is so denoted by an overbar. When expressed in terms of $\mathbf{a}_i$, the bar is absent. The sequence $k, i, \cdots, j$ is used to indicate that the nodes are numbered neither consecutively nor sequentially. The symbol $\bar{y}^*$ will be used to denote an arbitrary virtual displacement of the nodes.

Determination of U^* and W^* requires a knowledge of the oscillatory deformation field for the element. A standard procedure is to select a deformation function $\bar{w}$ of ξ, η, and ζ. The elements of the 3×1 vector $\bar{w}$ are the deformations parallel to axes ξ, η, and ζ and usually are chosen as polynomials in ξ, η, and ζ. Coefficients Γ_i for these polynomials are $6N$ in number where N is the number of nodes for the element. It is seen then that the number of coefficients matches the number of translational

[1]UCLA, Los Angeles, California.

[2]Likins, P. W., *Finite Element Appendage Equations for Hybrid Coordinate Dynamic Analysis* (JPL Technical Report to be published).

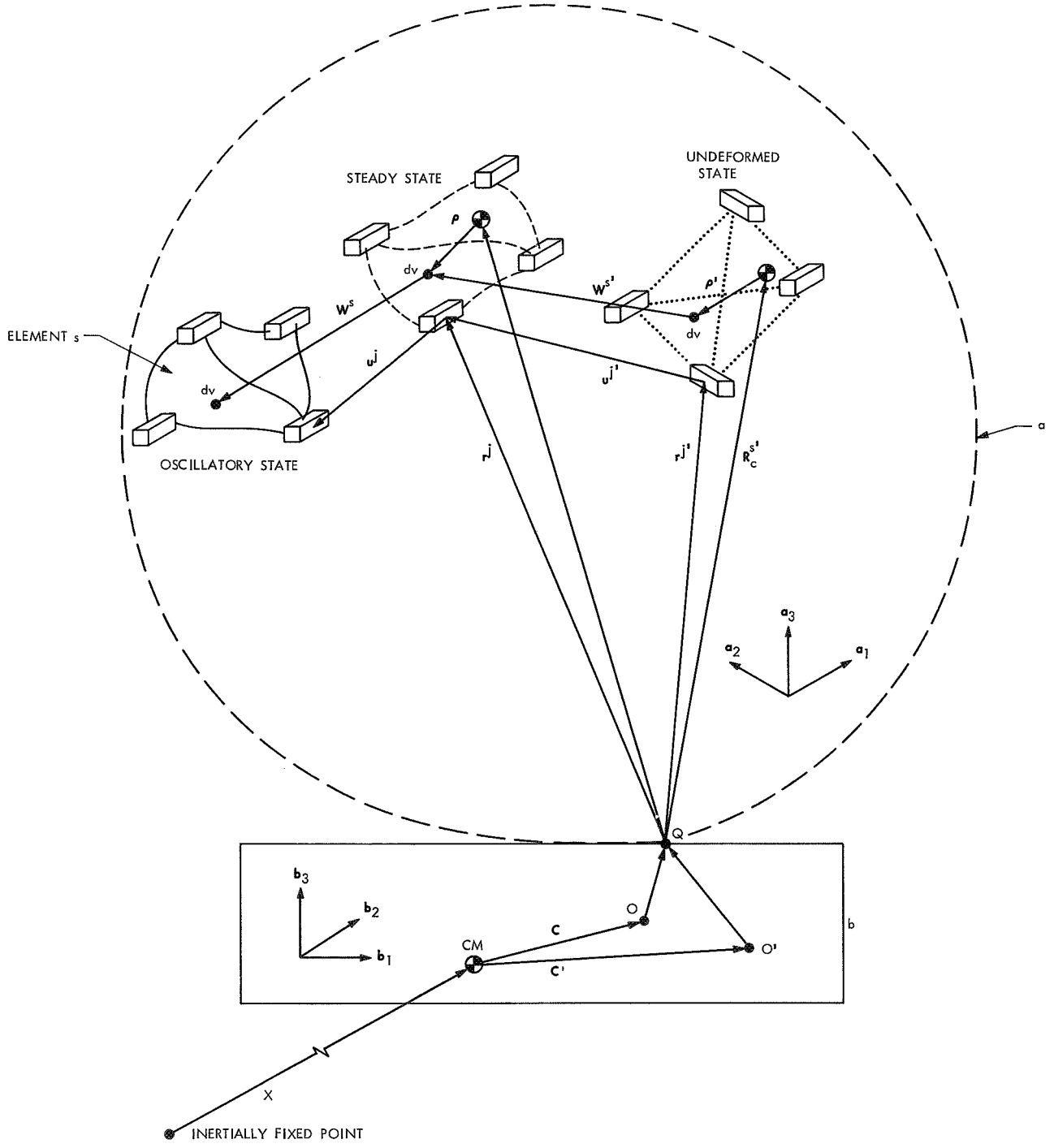

Fig. 1. Spacecraft model

and rotational displacements of the nodes. The deformation vector has the form

$$\bar{w} = P\,\Gamma \tag{2}$$

where

$$P = \begin{bmatrix} 1 & \xi & \eta & \zeta & \xi^2 & \xi\eta & \xi\zeta & \eta^2 \cdots 0 & 0 & 0 & 0 & 0 \cdots 0 & 0 & 0 & 0 \cdots \\ 0 & 0 & 0 & 0 & 0 & 0 & 0 & 0 \cdots 1 & \xi & \eta & \zeta & \xi^2 \cdots 0 & 0 & 0 & 0 \cdots \\ 0 & 0 & 0 & 0 & 0 & 0 & 0 & 0 \cdots 0 & 0 & 0 & 0 & 0 \cdots 1 & \xi & \eta & \zeta \cdots \end{bmatrix} \tag{3}$$

$$\Gamma = [\Gamma_1\,\Gamma_2 \cdots \Gamma_{6n}]^T \tag{4}$$

The partitioned sub-matrices of P are of size $3 \times 2N$. Before proceeding to the calculation of W^* and U^*, Γ must be determined. Equation (2) must apply to the nodes as well as to points within the element. Thus, for node j,

$$\bar{u}^j = \bar{w}(\xi_j, \eta_j, \zeta_j) = P(\xi_j, \eta_j, \zeta_j) \tag{5}$$

and

$$\bar{\beta}^j = \frac{1}{2}\,\tilde{\nabla}\,\bar{w}|_{\xi_j,\eta_j,\zeta_j} = \frac{1}{2}\,\tilde{\nabla}\,P|_{\xi_j,\eta_j,\zeta_j} \tag{6}$$

where

$$\tilde{\nabla} = \begin{bmatrix} 0 & -\partial/\partial\zeta & \partial/\partial\eta \\ \partial/\partial\zeta & 0 & -\partial/\partial\xi \\ -\partial/\partial\eta & \partial/\partial\xi & 0 \end{bmatrix} \tag{7}$$

Expressions of the type detailed in Eqs. (5) and (6) can be combined as follows:

$$\begin{bmatrix} \bar{u}^k \\ \bar{\beta}^k \\ \bar{u}^i \\ \bar{\beta}^i \\ \cdot \\ \cdot \\ \cdot \\ \bar{u}^j \\ \bar{\beta}^j \end{bmatrix} = \begin{bmatrix} P|_k \\ 1/2\,\tilde{\nabla}\,P|_k \\ P|_i \\ 1/2\,\tilde{\nabla}\,P|_i \\ \cdot \\ \cdot \\ \cdot \\ P|_j \\ 1/2\,\tilde{\nabla}\,P|_j \end{bmatrix} \Gamma \tag{8}$$

where $|_j$ implies evaluation at ξ_j, η_j, ζ_j, etc. If the matrix containing $P|_j$ and $\tilde{\nabla}\,P|_j$ terms is denoted F, then[3]

$$\bar{y} \underset{(1,8)}{=} F\,\Gamma \quad \Rightarrow \quad \Gamma = F^{-1}\bar{y} \tag{9}$$

[3]Numbers beneath equal signs indicate the equations referenced in writing the equation to which the equal sign corresponds.

and

$$\bar{w} \underset{(2,9)}{=} PF^{-1}\bar{y} \tag{10}$$

Define W as the matrix PF^{-1}. Then

$$\bar{w} = W\,\bar{y} \tag{11}$$

The deformation function is then a function of ξ, η, ζ and the nodal displacement vector.

A final step preparatory to the evaluation of the strain energy U^* is the determination of expressions for the variational stress and strain fields for the element. Variational stress and strain mean the increments in stress and strain beyond the steady-state value. It can be shown that the incremental strain in the element beyond any steady-state strain can be related to the deformation function $\bar{w}$ by

$$\bar{\varepsilon} = D\bar{w} \tag{12}$$

where

$$\bar{\varepsilon} = \begin{bmatrix} \bar{\varepsilon}_{11} \\ \bar{\varepsilon}_{22} \\ \bar{\varepsilon}_{33} \\ \bar{\varepsilon}_{12} \\ \bar{\varepsilon}_{23} \\ \bar{\varepsilon}_{13} \end{bmatrix}, \qquad D = \begin{bmatrix} \partial/\partial\xi & 0 & 0 \\ 0 & \partial/\partial\eta & 0 \\ 0 & 0 & \partial/\partial\zeta \\ \partial/\partial\eta & \partial/\partial\xi & 0 \\ 0 & \partial/\partial\zeta & \partial/\partial\eta \\ \partial/\partial\zeta & 0 & \partial/\partial\xi \end{bmatrix} \tag{13}$$

The variational thermal strain $\bar{\varepsilon}_T$ is

$$\bar{\varepsilon}_T = \bar{\alpha}\,T\,[1 \quad 1 \quad 1 \quad 0 \quad 0 \quad 0]^T \tag{14}$$

where T is the deviation in temperature from the steady state at a given point and $\bar{\alpha}$ is the coefficient of thermal

expansion. An expression for the variational stress is

$$\bar{\sigma} = S\,\bar{\varepsilon} - \bar{\sigma}_T \tag{15}$$

where the stress vector $\bar{\sigma}$ is

$$\bar{\sigma} = [\bar{\sigma}_{11}\ \bar{\sigma}_{22}\ \bar{\sigma}_{33}\ \bar{\sigma}_{12}\ \bar{\sigma}_{23}\ \bar{\sigma}_{31}]^T \tag{16}$$

and

$$S = \frac{E}{(1+2)(1-2\nu)}\begin{bmatrix} 1-\nu & \nu & \nu & 0 & 0 & 0 \\ \nu & 1-\nu & \nu & 0 & 0 & 0 \\ \nu & \nu & 1-\nu & 0 & 0 & 0 \\ 0 & 0 & 0 & (1-2\nu)/2 & 0 & 0 \\ 0 & 0 & 0 & 0 & (1-2\nu)/2 & 0 \\ 0 & 0 & 0 & 0 & 0 & (1-2\nu)/2 \end{bmatrix} \tag{17}$$

$$\bar{\sigma}^T = S\bar{\varepsilon}_T \tag{18}$$

E is the modulus of elasticity and ν is Poisson's ratio.

The expression for U^* is then

$$U^* = \int \bar{\varepsilon}^{*T}\bar{\sigma}dv = \bar{y}^{*T}\int W^T D^T S D W dv\bar{y} - \bar{y}^{*T}\int W^T D^T \bar{\sigma}_T dv \tag{19}$$

where dv is the differential element of volume of the finite element.

Work in deforming the element is done by inertial forces, body forces, forces exerted by nodal bodies, and surface forces. Distributing the surface forces to the nodes, as is ordinarily done, has the effect of eliminating them from the element equation. Denote the inertial force exerted on a differential element of the finite element by $-\mathrm{A}\mu\,dv$ where A is the acceleration of the mass center of the differential element, and μ is the mass density. Let $\bar{G}(\xi, \eta, \zeta)$ denote the body force for a generic point of the element. Finally, let $\bar{L}^s$ be the nodal body force vector for elements where

$$\bar{L}^s = [\bar{F}^{ks}\bar{T}^{ks}\ \cdots\ \bar{F}^{js}\bar{T}^{js}]^T \tag{20}$$

and $\bar{F}^{ks}$ and $\bar{T}^{ks}$ are 3×1 matrices in the local vector basis representing, respectively, the force and torque applied by the kth nodal body to the sth element. An expression for the work done is then

$$W^* = \bar{y}^{*T}\bar{L} + \int \bar{w}^{*T}\bar{G}dv - \int \bar{w}^{*T}\bar{A}\mu dv \tag{21}$$

where integration is carried out over the volume of the finite element and reference to element s is omitted. Equating W^* to U^* and use of the expression in Eq. (11) implies

$$\bar{L} = \int W^T D^T S D W dv\bar{y} + \int W^T [\bar{A}\mu - \bar{G} - D^T\bar{\sigma}_T]\,dv \tag{22}$$

After the evaluation of an expression for the acceleration $\bar{A}$, as in Ref. 1, the finite element equation takes the form

$$\begin{aligned}\bar{L}^s = {} & \bar{m}^s\ddot{\bar{y}} - \mathcal{M}_s W_c^{sT}\bar{C}^{sT}\frac{\left[\sum_{r=1}^{\epsilon}\bar{C}^{rT}\mathcal{M}_r W_c^r\ddot{\bar{y}}^r + \sum_{i=1}^{n} m_i\ddot{u}^i\right]}{\mathcal{M}} + \bar{g}^s\dot{\bar{y}}^s - 2\mathcal{M}_s W_c^{sT}\tilde{\bar{\omega}}^a\frac{\left[\sum_{r=1}^{\epsilon}\bar{C}^{rT}\mathcal{M}_r W_c^r\dot{\bar{y}}^r + \sum_{i=1}^{n} m_i u^i\right]}{\mathcal{M}} \\ & + (\bar{k}_0^s + \bar{k}_\Delta^s + \bar{\kappa}^s + \bar{\alpha}^s)\,\bar{y}^s - \mathcal{M}_s W_c^{sT}\bar{C}^{sT}(\tilde{\dot{\bar{\omega}}}^a + \tilde{\bar{\omega}}^a\tilde{\bar{\omega}}^a)\frac{\left[\sum_{r=1}^{\epsilon}\bar{C}^{rT}\mathcal{M}_r W_c^r\bar{y}^r + \sum_{i=1}^{n} m_i u^i\right]}{\mathcal{M}} + \int_s W^T\bar{C}(\tilde{\dot{\bar{\omega}}}^a + \tilde{\bar{\omega}}^a\tilde{\bar{\omega}}^a)\bar{C}^T\bar{\rho}\mu dv \\ & + \mathcal{M}_s W_c^{sT}\{\bar{C}^s C[\Theta\ddot{X} + (\tilde{\dot{\bar{\omega}}} + \tilde{\bar{\omega}}\tilde{\bar{\omega}})R] + \bar{C}^s(\tilde{\dot{\bar{\omega}}}^a + \tilde{\bar{\omega}}^a\tilde{\bar{\omega}}^a)R_c^s\} - \int_s W^T(\bar{G} - D^T\bar{\sigma}_T)\,dv\end{aligned} \tag{23}$$

New symbols introduced above have the following definitions:

$\bar{C}$ a 3×3 matrix relating $\mathbf{e}_i$ to $\mathbf{a}_i$ i.e., $\{e\} = C\{a\}$

g^s the element gyroscopic coupling matrix, i.e. $2\int W^T C\, \omega^a C^T W \mu dv$

$\bar{k}_0^s$ stiffness matrix for an unloaded element

$\bar{k}_\Delta^s$ preload stiffness matrix

$\mathcal{M}$ total vehicle mass

$\mathcal{M}_s$ mass of the sth element

m_i mass of the ith nodal body

$\bar{m}^s$ $\int_s W^T W \mu dv$, the consistent mass matrix

n number of nodal bodies

W_c^s the value of W^s when evaluated at the mass center ξ_c, η_c, ζ_c of element s

ϵ the number of finite elements

Θ a 3×3 matrix which transforms inertial coordinates to $\mathbf{a}_i$ coordinates

$\bar{\kappa}^s$ centrifugal stiffness matrix for finite element

$\bar{\rho}$ position vector of a differential element of volume of the finite element with respect to the element's mass center

ω^a the angular velocity of a relative to b

4. Nodal Body Equations of Motion

For nodal body j having mass m_j, inertial acceleration $\mathbf{A}^j$, inertia dyadic $\mathbf{I}^j$, and inertial angular velocity $\boldsymbol{\omega}^j$, the translational and rotational equations are

$$\mathbf{F}^j = m_j \mathbf{A}^j \tag{24}$$

$$\mathbf{T}^j = \mathbf{I}^j \cdot \boldsymbol{\omega}^j + \boldsymbol{\omega}^j \times \mathbf{I}^j \cdot \boldsymbol{\omega}^j \tag{25}$$

By using procedures outlined in *Section IIIB* of Ref. 1, it can be shown that Eqs. (24) and (25) have the more detailed forms

$$f^j - \sum_{s \epsilon \epsilon_j} \bar{C}^{sT} \bar{F}^{js} = m^j \left\{ C\Theta \ddot{X} + C\left[\ddot{e} + 2\tilde{\omega}\dot{e} + (\dot{\tilde{\omega}} + \tilde{\omega}\tilde{\omega})\, e\right] + (\dot{\tilde{\omega}}^a + \tilde{\omega}^a\tilde{\omega}^a)\, r^j + \ddot{u}^j - \frac{\left(\sum_{i=1}^{n} m^i \ddot{u}^i + \sum_{r=1}^{\epsilon} \bar{C}^{rT} \mathcal{M}_r W_c^r \ddot{\bar{y}}^r\right)}{\mathcal{M}} \right.$$

$$\left. + 2\tilde{\omega}^a \left[\dot{u}^j - \frac{\left(\sum_{i=1}^{n} m^i \dot{u}^i + \sum_{r=1}^{\epsilon} \bar{C}^{rT} \mathcal{M}_r W_c^r \dot{\bar{y}}^r\right)}{\mathcal{M}} \right] + (\dot{\tilde{\omega}}^a + \tilde{\omega}^a\tilde{\omega}^a) \left[u^j - \frac{\left(\sum_{i=1}^{n} m^i u^i + \sum_{r=1}^{\epsilon} \bar{C}^{rT} \mathcal{M}_r W_c^r \bar{y}^r\right)}{\mathcal{M}} \right] \right\},$$

$$j = 1, \cdots, n \tag{26}$$

$$\tau^j - \sum_{s \epsilon \epsilon_j} \bar{C}^{sT} \bar{T}^{js} = I^j \dot{\omega}^a + \tilde{\omega}^a I^j \omega^a + I^j \ddot{\beta}^j + \left[\tilde{\omega}^a I^j - (I^j \omega^a)\tilde{} + I^j \tilde{\omega}^a\right] \dot{\beta}^j + \left[I^j \dot{\tilde{\omega}}^a - (I^j \dot{\omega}^a)\tilde{} + \tilde{\omega}^a I^j \tilde{\omega}^a - \tilde{\omega}^a (I^j \omega^a)\tilde{}\,\right] \beta^j \tag{27}$$

Reference 1 or a report to be published (Footnote 2) should be consulted for the definition of any new symbols. Substitution of the expressions in Eqs. (20) and (23) for $\bar{F}^{js}$ and $\bar{T}^{js}$ into Eqs. (26) and (27) produces a complete set of dynamical equations for the appendage.

Combining of Eqs. (20), (23), (26), and (27) produces an equation of the form

$$M'\ddot{q} + D'\dot{q} + G'\dot{q} + K'q + A'q = L' \tag{28}$$

where

$$q = [u_1^1 u_2^1 u_3^1 \beta_1^1 \beta_2^1 \beta_3^1 \cdots \beta_3^n]^T \tag{29}$$

is the matrix of nodal deformation coordinates. M', D', and K' are symmetric while G' and A' are skew symmetric and L' is a $6n \times 1$ matrix.

In more detail,

$$M' = M + M^c - M^* \tag{30}$$

where M is null except for the 3×3 matrices m^1, I^1, m^2, $\cdots$ I^n associated with the nodal bodies along its principal diagonal, M^c is the consistent mass matrix associated with the finite elements, and $-M^*$ accommodates the reduction of the effective inertia matrix due to mass center shifts within the vehicle induced by deformation.

Actually, the term $D'\dot{q}$ does not result through combining Eqs. (20), (23), (26), and (27) but is an artifice introduced to account for structural damping. This procedure is common practice in structural dynamics analyses and its validity will not be discussed here. G' is a function of ω^a and is referred to as the gyroscopic coupling term. Three types of terms contribute to K'. They are $\bar{k}_0^s$, k_Δ, and $\bar{\kappa}^s$. All remaining terms in q comprise A'. L' is the matrix of externally applied forces and torques.

5. Summary

A brief synopsis of the dynamics analysis for an improved model of a spacecraft flexible appendage has been presented. The appendage matrix equation of motion, Eq. (28), is similar in form to Eq. (84) of Ref. 1. However, new interpretations must be given to each term. Equation (28) must be augmented by the vehicle equations of motion as described in *Section IIIC* of Ref. 1 and by the control system equations described in *Section V* of Ref. 1.

Equation (28) is rather unwieldy as it stands. Simplifications must be made in order for the appendage equations to have real utility. Such simplifications are discussed in the latter part of a report to be published (Footnote 1). In particular, coordinate transformations are suggested which will permit the replacement of the homogeneous form of Eq. (28) with a set of completely uncoupled differential equations. Reducing the number of these equations by truncation, when justified, permits further simplification of the appendage equations.

Reference

1. Likins, P. W., *Dynamics and Control of Flexible Space Vehicles*, Technical Report 32-1329. Jet Propulsion Laboratory, Pasadena, Calif., Jan. 15, 1970.

C. Digital Gyro System (Phase I), *P. J. Hand*

A digital gyro system has been developed, built, and tested by the Inertial Sensors Group for the thermoelectric outer planet spacecraft (TOPS) single-axis simulator. The serial digital position information from this system will be used to stabilize the digital attitude-control system and will provide accurate commanded turn capability for the single-axis simulator.

The breadboard electrical design described in SPS 37-59, Vol. III, pp. 130–132, has been modified and packaged into a single unit containing the gyro, the electronic rebalance loop, and the dc-to-dc power converters. The system is self-contained and requires only 30-V, 0.7-A dc power. The output interface is a two-wire (positive $\Delta\theta$ and negative $\Delta\theta$) line to the attitude-control electronics package. The output circuits utilize low-power transistor–transistor logic integrated circuits with a pulse scale factor of 0.001 deg/pulse. Gyro capture capability is maintained up to 1.2 deg/s of input rate.

The gyro, described in SPS 37-59, Vol. III, is a Honeywell Inc., type GG334S, and was recently rebuilt by Honeywell for use with this digital system. The complete digital gyro system for installation on the single-axis simulator is shown in Fig. 1. The top and side covers were removed (Fig. 1b) to show the location of the internal parts. The gyro is in the rectangular box on the left, the plug-in electronics cards are in the center, and the two dc-to-dc converters are on the right, outside the main chassis. The dc-to-dc converters were designed and supplied by the Power Subsystems Group.

This complete gyro system has been extensively tested since August 1970. During the testing, the gyro was oriented as it will be in the simulator, as an azimuth gyro, i.e., with the gyro input axis vertical. As of October 15, 1970, 930 h of operating time had been accrued. Daily runs have been made to determine the drift characteristics of the gyro and the pulse scale factor of the gyro system. A plot of these data is shown in Fig. 2. The points

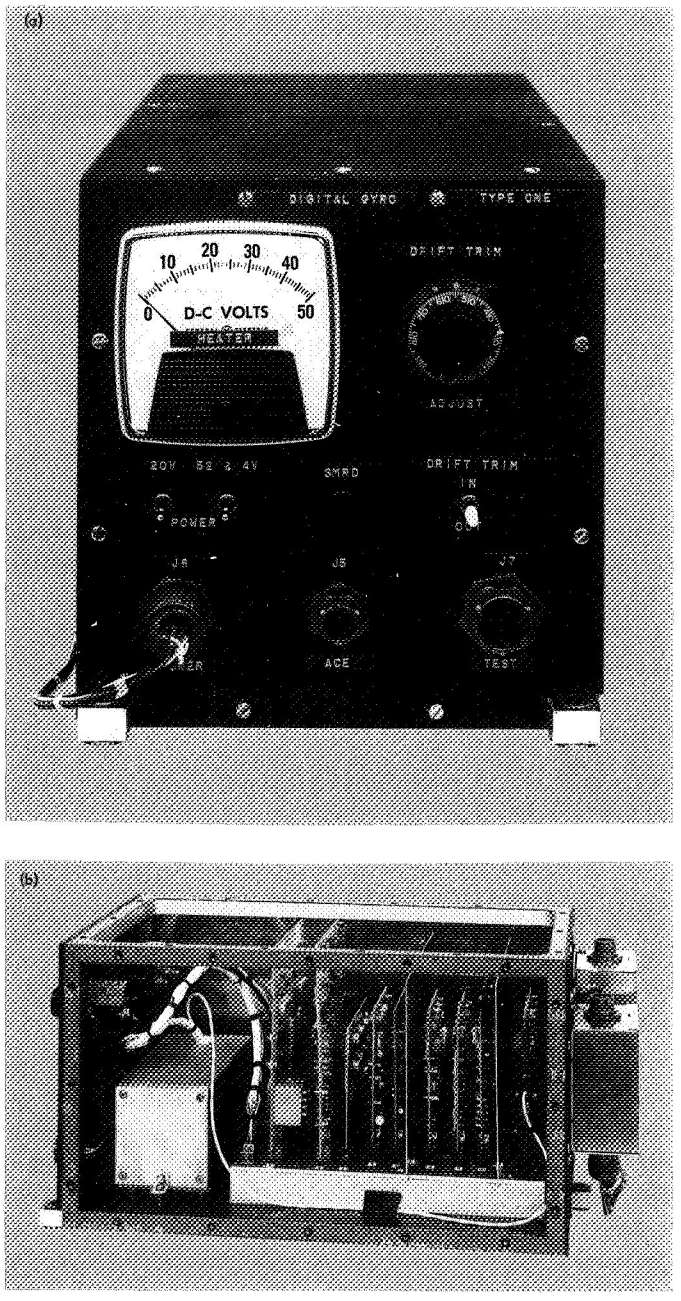

Fig. 1. Digital gyro system: (a) front view, (b) internal view, top and side covers removed

represent the average for one day's run, which may contain from 2 to 30 readings of the gyro's output with vertical earth's rate input. The curve plotted as composite drift rate error is the difference between the measured gyro output and the actual value of 8.45497 deg/h (JPL vertical earth rate component). This drift is actually due to the composite effects of gyro spin axis mass unbalance, fixed torques, and pulse scale factor variations. It is indicative of the stability of this gyro system on a day-to-day basis. The data has a range of 0.60 deg/h, which is representative of the performance of the GG334S model gyros. An increasing trend is also present in the drift data, which was also noted in previous testing of other gyros of this model.

Observation of Fig. 2 indicates that the pulse scale factor is slowly decreasing with increasing operating time; however, this trend appears to be stabilizing. The pulse scale factor stability is affected by both the gyro command rate scale factor stability and the digital loop electronics stability. The digital loop parameters were monitored carefully during this test period and did not change, so it is probable that the pulse scale factor trend is due to changes in the gyro command rate scale factor.

When used on the single-axis simulator, the gyro system will be trimmed to null-out both the effect of vertical earth's rate and the composite drift rate term. This will be accomplished by injecting a small analog current into the gyro torquer. The gyro will then only be sensing motions of the simulator. However, this nulling of the major drift input cannot take care of the short-term random drift effect of the gyro. Figure 3 is a plot of one typical day of drift, showing the random drift effect. The data were obtained by totalizing $\Delta\theta$ pulses for 1000-s periods during a normal working day. Random drift is a non-systematic time varying component of drift rate measured under controlled operating conditions. It is normally expressed as the standard deviation of the gyro output over a specified period of time. The standard deviation of the one-day run shown in Fig. 3 is 0.021 deg/h. The data range is 0.069 deg/h and the average value is +1.260 deg/h.

It is planned that the gyro system will run continuously, even when the simulator is not operating, to eliminate the long warm-up time characteristics associated with this model gyro. The composite drift will then be adjusted to as near zero as is practical, just before a simulator run is started. In this manner, only the gyro short-term random drift will affect the simulator system. A random drift of 0.021 deg/h is acceptable for the simulator system application.

The Phase I system was developed to demonstrate this simplified digital torquing technique on the single-axis simulator. Continued development of this concept is planned, using newer, high reliability, low-power microcircuitry. Simpler circuit designs will be investigated and the final circuit will be tailored to function with a smaller, lower-powered, and more accurate gyro than the GG334S used in the Phase I system.

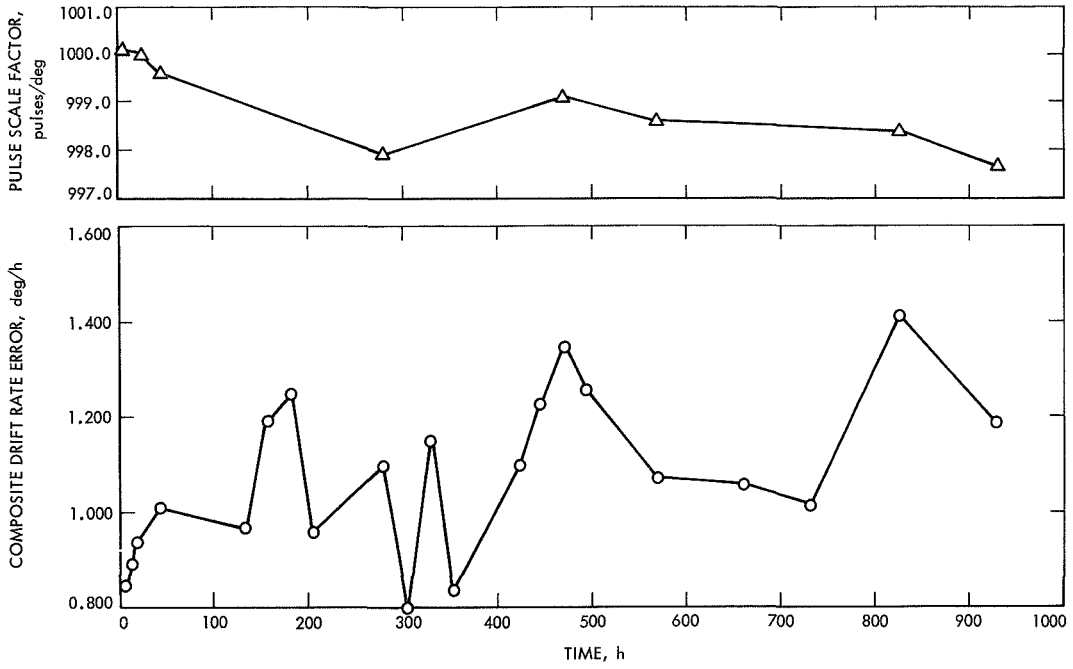

Fig. 2. Digital gyro system performance vs running time

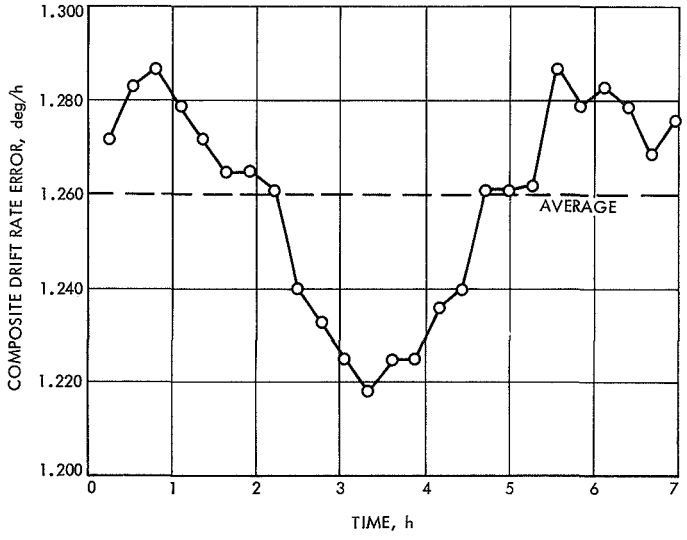

Fig. 3. Digital gyro system drift vs time (1-day run time at start = 495.3 h; 1000-s integration time)

D. Stepper Motor Drive Electronics for the Solar Electric Thrust Vector Control Subsystem,

W. E. Crawford

1. Introduction

One of the tasks required to complete the solar electric thrust vector control electronics has been the design of a stepper motor drive system. The location of the composite ion engine thrust vector is controlled by translator and gimbal actuators that use a stepper motor as the driving element. The stepper motors chosen for the actuators are 90 deg/step permanent magnet motors that feature a magnetic detent at each step. This detent allows the stepper motor to be operated in a pulse fashion rather than having the stepper motor windings continuously powered. This feature results in a significant power saving since the stepper motor duty cycle is low in the solar electric thrust vector control subsystem.

Commercially available stepper motor driver electronics have three characteristics that make them unacceptable for the thrust vector control. These are:

(1) The windings are continuously powered, therefore, wasteful of power.

(2) The electronics has a latch-up mode that is correctable only by removing the power supply voltage.

(3) The reliability of the electronic components is unknown.

The design detailed in this article corrects all of the undesirable features.

2. Circuit Description

Figure 1 shows a schematic of the stepper motor driver electronics. The diagram contains the following circuits:

(1) Power driver switches to the motor windings.

(2) Clock pulse generator.

(3) Four-bit ring counter.

(4) Logic for the ring counter.

The power drivers are a Darlington pair comprised of 2N2222 and SDT 5003 transistors. The Darlington circuit is driven by a series 54L *nand* gate. The circuits shown on this schematic use series 54L transistor–transistor logic microcircuits exclusively because of the low power requirements.

The function of the clock circuit is to delay the clock pulse to the ring counter for a few microseconds, long enough for the ring counter logic to set.

The four-bit ring counter, along with the ring counter logic, transfers a logical "1" either clockwise or counterclockwise each time a clockwise or counterclockwise pulse appears at the input. The outputs of the ring counter are fed into the motor winding driver circuits in order to drive the stepper motor in either direction.

The ring counter and ring counter logic are complex in order to overcome the "latch-up" feature of commercial stepper motor drivers. This circuit has an error correcting logic in case an unacceptable state appears in the ring counter. Unacceptable states can appear in the ring counter as a result of turn-on transients and power supply transients. Table 1 shows the logical behavior of the ring counter for both acceptable and unacceptable states. The ring counter is comprised of series 54L73 dual J-K flip flops. The formulas for the J-K inputs are shown below:

$$J_A = B\bar{D}E + D\bar{E}, \qquad K_A = 1$$

$$J_B = AD + A\bar{E} + \bar{A}DE, \qquad K_B = \bar{A} + \bar{D}$$

$$J_C = B\overline{DE} + \bar{A}DE, \qquad K_C = \bar{J}_C$$

$$J_D = \overline{ABE} + AE, \qquad K_D = 1$$

Table 1. Ring counter logic

N	Clockwise N + 1	Counterclockwise N + 1
ABCD	ABCD	ABCD
Acceptable states: 1000	0001	0100
Acceptable states: 0100	1000	0010
Acceptable states: 0010	0100	0001
Acceptable states: 0001	0010	1000
Unacceptable states: 0000	Acceptable states: 0100	Acceptable states: 0010
Unacceptable states: 1111	0100	0100
Unacceptable states: 1110	0001	0010
Unacceptable states: 1101	0100	0100
Unacceptable states: 1011	0100	0100
Unacceptable states: 0111	0010	1000
Unacceptable states: 0011	0010	1000
Unacceptable states: 1001	0100	0100
Unacceptable states: 1100	0001	0010
Unacceptable states: 0110	1000	0010
Unacceptable states: 1010	0001	0100
Unacceptable states: 0101	0010	1000

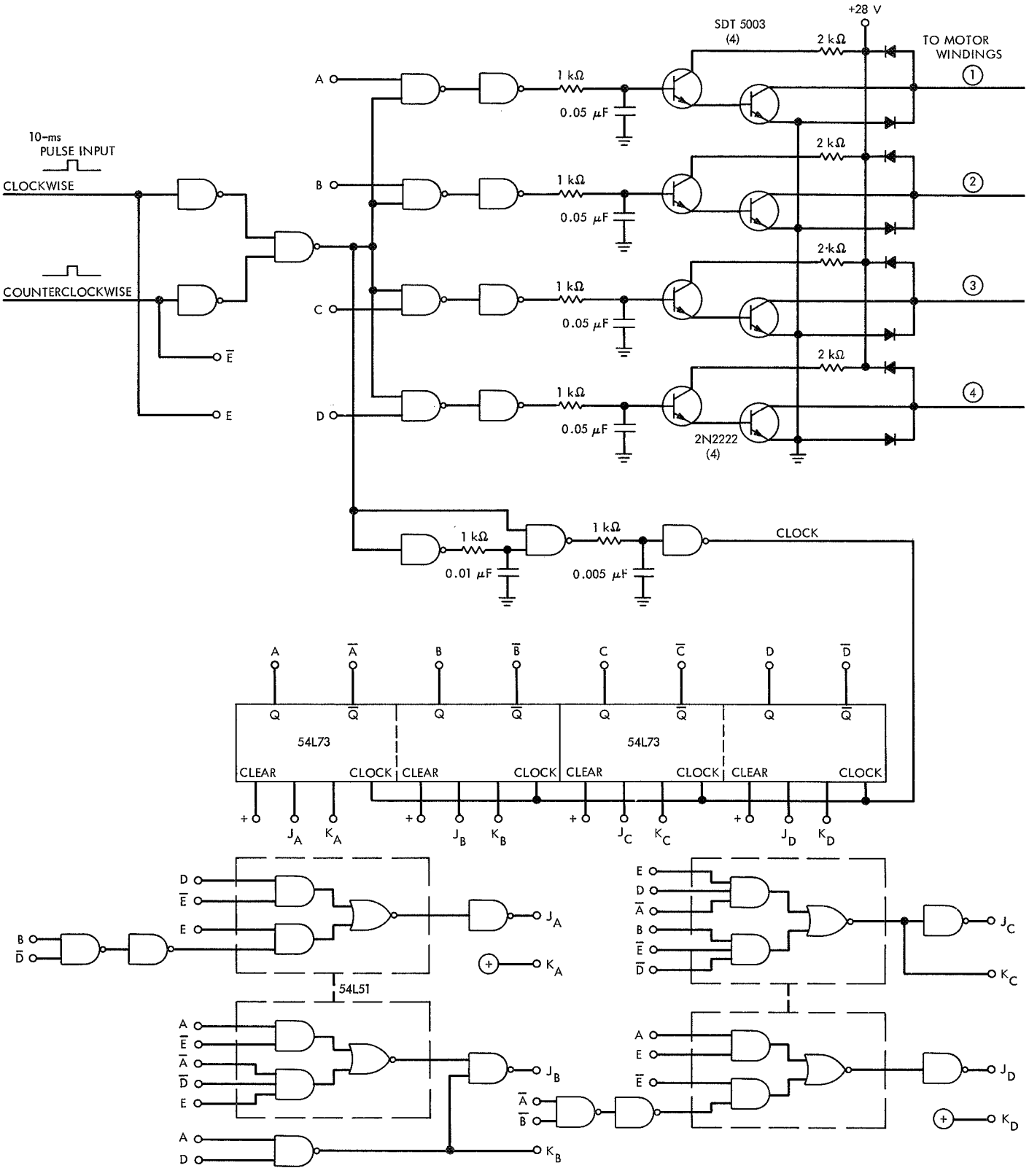

Fig. 1. Stepper motor driver electronics

3. Conclusion

The circuits described in this article have been breadboarded and tested and are now incorporated in the solar electric closed-loop thrust vector control system. This system uses six stepper motor driver electronics, two for translator actuators and four for the gimbal actuators. Figure 2 shows two stepper motor driver electronics packaged on a printed circuit board. As can be seen from Fig. 2, each driver requires nine flat-packs, eight transistors, and a few additional discrete parts. The circuit design, as shown in Fig. 1, uses very little power, is free from "latch-up" states, and uses high reliability components.

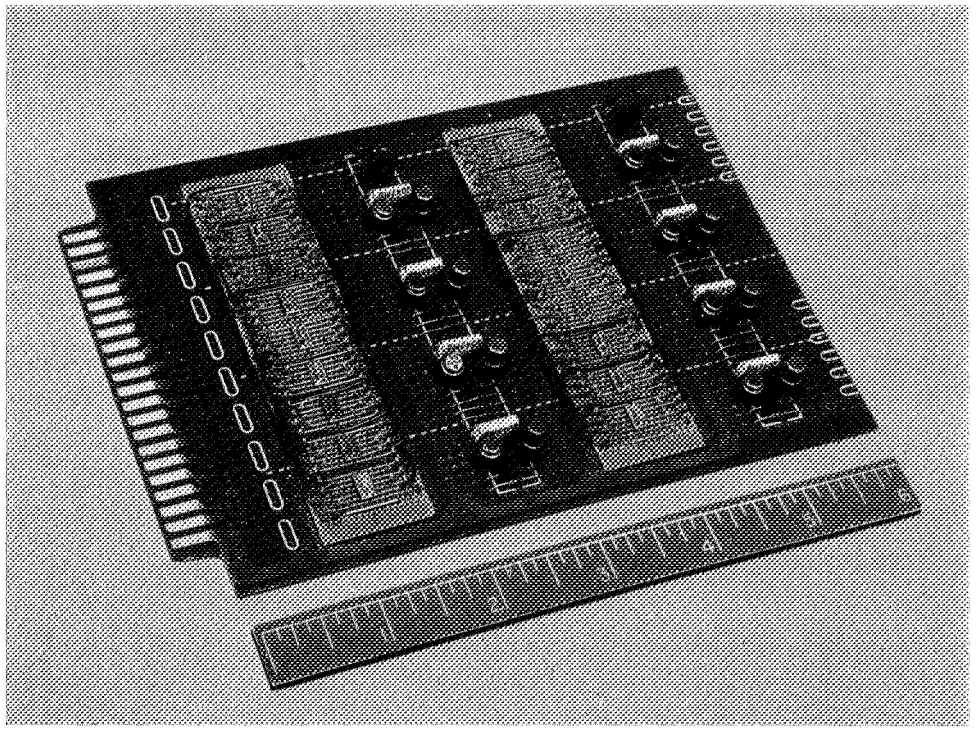

Fig. 2. Printed circuit board of two stepper motor driver electronics